Talon–P: CFD Simulations

Matthew Dean*, Benjamin Derks†, and Jonathan Poggie‡
Purdue University, West Lafayette, IN, 47906

This paper is a contribution to a special session focused on the analysis and optimization of a vehicle inspired by the Stratolaunch Talon–A vehicle, the baseline case of which we will refer to as Talon-P. Mach 6.0 flow over a generic boost glide vehicle was investigated through laminar CFD simulations. Comparisons were made between simulated results and experimental data collected in Purdue University's BAM6QT hypersonic tunnel. Similar surface heating patterns, such as streaks on the lower and upper surfaces of the vehicle, were observed both in CFD simulations and experimental infrared imaging. Six different nose geometries were investigated, and overall good agreement between the experimental and simulated results was observed. Two configurations of the Talon-P experienced substantial disagreement between simulated predictions and experimental results; possible reasons for these discrepancies are discussed. The effect of nose geometry on downstream flow behavior is also investigated, with special emphasis on the vortical structures which form near the nose on the bottom surface of the geometry. The CFD results presented in this paper are part of a larger design, downselection, and analysis process.

I. Introduction

STRONG boundary-layer gradients in hypersonic flows give rise to intense skin friction, surface heating, and pressure changes [1–16]. For hypersonic flight vehicles, sharp windward surfaces located behind shocks are generally subjected to the greatest heating of any point on the body surface [1, 5, 8, 10, 11, 17–21]. In hypersonic glide vehicle (HGV) configurations, thin wings and fins are advantageous for producing high lift-to-drag ratios, but result in undesirable aerothermal performance. Therefore, it is essential to study the external flow over HGV bodies as part of the design process to mitigate damage to surface materials and sensitive instrumentation. Purdue University's generic derivative of the Stratolaunch Talon-A vehicle, the Talon-P, provides a plausible hypersonic glide boost vehicle configuration for computational and experimental studies. Performing high-fidelity computational fluid dynamics (CFD) simulations of the Talon-P geometry helps identify the aerodynamic and aerothermal behaviors of the Talon-P and Talon-P variations. In the broader scope of the Design/Test/Build/Fly (DTBF) cycle, CFD simulations provide a relatively inexpensive way to evaluate the performance of various designs during the early phases of the DTBF cycle. Specifically, CFD may be used to evaluate lift, drag, thermal protection system requirements, large-scale flow unsteadiness, etc. to determine the advantages and disadvantages of several designs. The studies discussed in this paper are part of a broader downselection and design effort.

The downselection process involved generating a large initial pool of geometry candidates. Full CAD geometries of the vehicle were generated for each nose configuration and run using the Configuration-Based Aerodynamics (CBAero) software. CBAero is a low-fidelity panel method software primarily used to estimate the aerodynamic and aerothermal performance of a given geometry. CBAero offers the advantage of very low computational costs while sacrificing the fidelity of CFD predictions. In the downselection process, CBAero was used to determine force and moment coefficients for each nose configuration. Five noses were selected from the larger pool of initial candidates to obtain a range of unique aerodynamic and aerothermal behaviors. High-fidelity CFD simulations of the baseline geometry were used to validate preliminary CBAero results during the early phases of the project.

The costs associated with running CFD simulations were evaluated over the course of the project. Generally, the financial costs of building, operating, and maintaining supercomputing resources is a significant investment. Unless there is a persistent need for supercomputing resources, this investment is difficult to justify for most organizations. For this reason, it is usually easier to purchase computing time on or rent a portion of a pre-existing HPC system. For this DTBF cycle time analysis, it is easiest to describe the costs associated with running CFD simulations in terms of computer hour usage. One computer hour corresponds to a task running on one computing core for a full hour; a

*Graduate Research Assistant, Department of Aeronautics and Astronautics.
†CFD M&S Applications Research Engineer, CFD Research Corporation.
‡Professor, Department of Aeronautics and Astronautics. AIAA Associate Fellow.

task run on 128 cores for a full hour would use 128 computing hours. For the simulations run over the course of this project, each simulation ran on 5120 computing cores for roughly 24 hours until simulation convergence was reached, for a total of 122,880 computing hours per computation. Simulations were run for all six nose configurations, giving us a minimum computer hour usage estimate of 737,280. Generally, it is expected that CFD simulations will require at least two attempts to achieve a satisfactory solution. This is especially true of complex geometries where several attempts may be needed to get proper resolution of irregular geometric features. Over the course of this project, all meshes required minor adjustments to get good quality at two problematic areas: the nose tip and the root of the wing leading edges. Increasing our minimum estimate by a factor of 5 gives us roughly 3.7 million computer hours, which is likely closer to the total computer hour usage for this project. The expenses associated with running CFD may range widely depending on the complexity of the geometry and the experience level of the CFD user.

Significant effort on this project has focused on obtaining experimental results for the downselected nose geometries. Experiments were carried out in the Boeing – Air Force Office of Scientific Research Mach 6 Quiet Tunnel (BAM6QT) at Purdue University. The BAM6QT is a blow-down wind tunnel which can produce quiet laminar flow at hypsersonic freestream velocities. Many existing hypersonic tunnels observe significant freestream acoustic noise in the test section due to turbulence generated in the upstream boundary-layer along the wall of the tunnel. Turbulent incoming flow prohibits the accurate study of boundary-layer transition on the test model. The BAM6QT uses various techniques to mitigate boundary-layer turbulence upstream of the test section, allowing for a more accurate study of boundary-layer transition on the model. The experimental effort on this project helps to provide a physical basis for the high-fidelity CFD and low-fidelity CBAero studies. More information about the BAM6QT, experimental methodology, and experimental results can be found in [22].

The HGV configuration offers many advantages for atmospheric hypersonic flight. Specifically, high lift-to-drag ratios and smooth integration of airframe and propulsion components makes the waverider design an attractive choice for hypersonic flight applications [23–25]. The use of waverider configurations has been explored for a variety of applications, including: atmospheric reentry, rocket-powered hypersonic flight, and air-breathing hypersonic flight [23–25]. The high lift-to-drag ratio of the waverider configuration makes the design desirable for re-entry flight. The craft may begin at very high angles-of-attack to maximize drag and reduce craft velocity during the initial reentry phases. At high angles-of-attack, the bottom surface of the waverider serves as a heat shield, similar to ones used on reentry capsule configurations. The main advantage of high lift-to-drag waverider configurations over capsule configurations is that the waverider can transition to lower angles-of-attack and enter a controlled glide phase in the lower atmosphere. This paper will focus on an example HGV geometry, the Talon-P, along with five nose variations of the Talon-P configuration. Comparisons between experimental and simulated results assist in validating simulated results. This paper will also analyze the simulated results for each geometry, with specific focus on how altering the nose geometry produces changes in the downstream flow.

II. Methodology

A. Configuration and Flow Conditions

The geometry of interest is a hypersonic glide boost vehicle similar to the Talon-A vehicle developed by Stratolaunch LLC. The baseline Talon-P configuration was developed independently by the Purdue University team from publicly released images of the Stratolaunch Talon-A vehicle. The nose of the Talon-P geometry is interchangeable to create different configurations of interest. Figure 1 displays an overall view of the baseline nose configuration, along with terminology that will be used in this paper to describe components of the waverider vehicle. The nose/body interface shown in Fig. 1 is the location where the nose can be detached from the rest of the body and replaced with other variations of the nose.

Six nose geometries were investigated, shown in Fig. 2. The Baseline geometry is the most similar to Stratolaunch's Talon-A vehicle, and Samples 2, 3, 9, 12, and 13 are variations of the same vehicle with a different nose geometry. The Sample nose geometries were chosen from a broader pool of potential nose geometries during the downselection process. The downselection process involved generating a broad range of possible noses within given size and shape constraints. For all generated nose designs, the nose/body interface is smooth and continuous on the upper surface of the vehicle, and continuous with a change in slope on the bottom surface. Noses with infeasible designs were discarded after this process. The Configuration-Based Aerodynamics (CBAero) and Kestrel Computational Fluid Dynamics (KCFD) software were then used to further narrow down the nose geometries based on lift and moment coefficients along with the aerothermal performance of each geometry. In cases where multiple nose geometries exhibited very

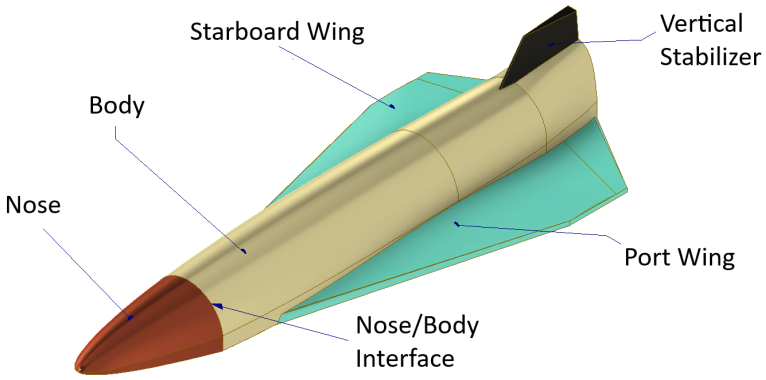

Fig. 1 Talon-P baseline geometry. General schematic with important sections labeled.

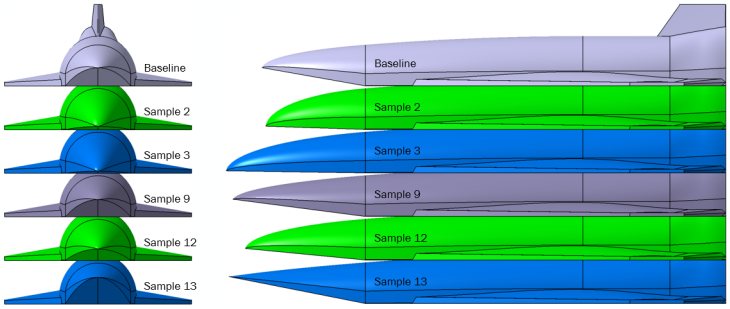

Fig. 2 Baseline and five Sample nose geometries.

Table 1 Wind tunnel conditions.

$M_\infty = 6.0$
$P_\infty = 483$ Pa
$T_\infty = 50$ K
$T_w = 298$ K

similar aerodynamic performance, one was selected and the others were eliminated. The final Sample nose geometries shown in Fig. 2 are the geometries that remain after the downselection process. The Sample nose geometries were selected to provide a wide range of aerodynamic performances for analytical purposes. More information about the downselection process is available in [22].

The freestream flow conditions that will be used for all simulations are given in Table 1. These conditions are based on the approximate conditions achieved by Purdue University's Boeing - Air Force Office of Scientific Research Mach 6 Quiet Tunnel (BAM6QT). The measured static freestream pressure, P_∞, varies slightly between wind tunnel runs (±20 Pa). To keep consistency between CFD runs, an average static freestream pressure of 483 Pa was used. The freestream gas is air, assumed to be calorically perfect for all simulations; this is a reasonable assumption given the near-cryogenic operating temperatures of the BAM6QT. Freestream vibrational non-equilibrium due to freezing of the vibrational energy modes near the tunnel throat was neglected in all simulations.

B. Mesh Design

Meshes were generated using Pointwise version 18.6 software, developed by Cadence Design Systems, Inc. [26]. All meshes are generated using the anisotropic tetrahedral extrusion (T-Rex) method. The initial wall spacing is 2.0×10^{-6} m with a growth rate of 1.10 per layer. The initial boundary layer spacing and growth rate were chosen to target Δy^+ values

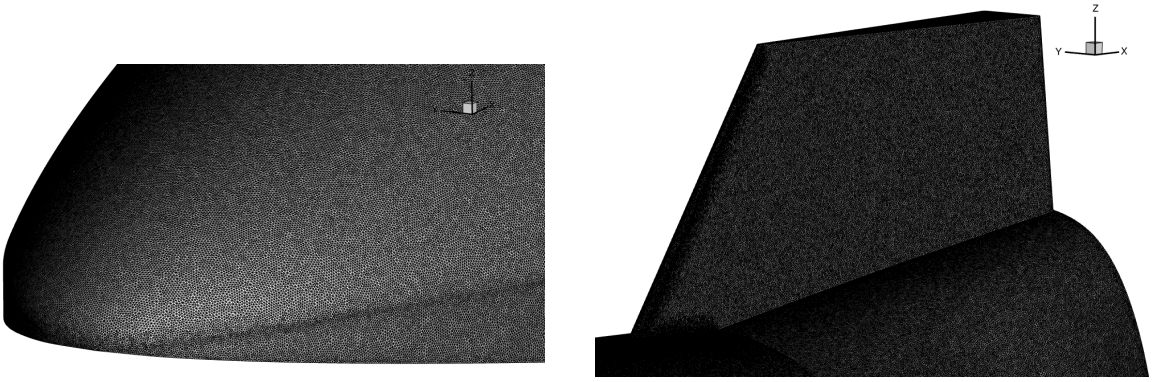

(a) **(b)**

Fig. 3 Baseline mesh design. (a) Nose closeup. (b) Vertical stabilizer closeup.

less than 1 across the body surface. Approximately 50 anisotropic cell layers are generated in the boundary-layer region, and the rest of the domain is filled with tetrahedral cells. A different mesh was generated for each nose configuration. All meshes contain approximately 300 million total cells. Figure 3 displays the surface mesh resolution on the nose (LHS plot) and the rear vertical stabilizer (RHS plot) on the baseline geometry. The mesh was designed such that the farfield inflow boundary does not interfere with the initial shock location. At the outflow mesh boundary, the flow was ensured to be fully supersonic in all simulations.

C. Laminar Simulation Methods

Simulations were carried out using the CREATE-AV Kestrel CFD software provided by the DoD's High Performance Computing Modernization Program [27, 28]. Kestrel Computational Fluid Dynamics (KCFD) is an unstructured, finite volume flow solver. Simulations were carried out on DoD High Performance Computing systems, using 5120 computing cores and approximately 24 hours for each simulation to reach 20,000 total iterations.

Steady-state simulations in Kestrel are carried out using a Courant–Friedrichs–Lewy (CFL)–based local time stepping scheme. The CFL value is initially set to 1 and slowly increased to 1000 over the course of the 10,000 startup iterations. This method of CFL ramping helps to avoid issues with transient behaviors at the beginning of the simulations. The simulation is then run for 10,000 iterations with a CFL value of 1000 until convergence. Convergence was determined by low mass, momentum, and energy equation residuals along with negligible changes in skin friction and surface heat flux. A value of 0.05 was used for Kestrel's advective temporal damping parameter to help damp spurious solution changes that occur during early simulation transients. The HLLE++ scheme was used to compute the inviscid fluxes, the Alpha-Damping [29] scheme was used to compute the viscous fluxes, and the Van Leer scheme was used to compute the viscous flux Jacobians [30]. Kestrel utilizes a flux limiter method similar to the Barth-Jespersen flux limiter for flux computations [31]. All simulations were carried out using a second-order finite volume spatial discretization method of the Navier-Stokes equations. The conservative form of the Navier-Stokes equations is given by Eq. 1. $\bar{U}$ is the solution vector of mass, momentum, and energy. $\bar{F}_c$ and $\bar{F}_v$ represent the convective and viscous fluxes, respectively. $\bar{S}$ is the source term vector and is zero for all simulations in this paper.

$$\frac{\partial \bar{U}}{\partial t} + \nabla \cdot \bar{F}_c - \nabla \cdot \bar{F}_v - \bar{S} = 0$$

$$\bar{U} = \begin{bmatrix} \rho \\ \rho\bar{v} \\ \rho E \end{bmatrix}, \qquad \bar{F}_c = \begin{bmatrix} \rho\bar{v} \\ \rho\bar{v}\bar{v}^T + \bar{\bar{I}}P \\ \rho E\bar{v} + P\bar{v} \end{bmatrix}, \qquad \bar{F}_v = \begin{bmatrix} 0 \\ \bar{\bar{\tau}} \\ \bar{\bar{\tau}} \cdot \bar{v} + \kappa\nabla T \end{bmatrix} \tag{1}$$

For all simulations, the wall is modeled using Kestrel's no-slip, isothermal wall boudnary condition. The no-slip condition ensures that the velocity at the wall is zero in all directions tangent to the wall. The domain inflow and outflow are modeled using Kestrel's default modified Riemann invariant far-field boundary scheme.

The majority of the simulation work shown in this paper assumed a laminar flow, that is, directly solving Eq. 1 without applying turbulence or transition models in the boundary-layer region. The experimental results displayed in Section III.A indicate a flow that is laminar, helping to validate the laminar flow assumption made for the simulations. For completeness, some preliminary CFD work performed with the Reynolds-Averaged Navier-Stokes (RANS) equations with transition and turbulence models included is presented in Section III.C. The transitional RANS methodology is described in Section II.D. Generally, the transitional RANS methods over-predicted transitional behavior in the boundary-layer flow when compared with experimental results. A discussion of the incorrect RANS results is presented in Ref. III.C.

D. RANS Simulation Methods

In RANS CFD modeling, turbulent boundary-layer eddies are not resolved to help significantly reduce computation time. Instead, a turbulence model is applied which approximates a time-averaged turbulent boundary layer profile in the near-wall region. For simulations presented in this paper, the Menter 1-equation transition model and the compressible Spalart-Allmaras (SA) turbulence model were used to model boundary layer transition from laminar to turbulent flow. The main SA turbulence model equation solved by KCFD is given by Eq. 2. In this equation, $\tilde{\nu}$ is the turbulence variable, μ_t is the turbulent eddy viscosity, and $\hat{S}$ is the turbulence production term. Supplemental constant and equations used by KCFD to solve Eq. 2 are located in [32, 33].

$$\frac{\partial \tilde{\nu}}{\partial t} + U_i \frac{\partial \tilde{\nu}}{\partial x_i} = c_{b1}(1 - f_{t2})\hat{S}\tilde{\nu} - \left[c_{w1} f_w \frac{c_{b1}}{\kappa^2} f_{t2}\right]\left(\frac{\tilde{\nu}}{d_w}\right)^2 + \frac{1}{\sigma}\left[\frac{\partial}{\partial x_i}\left((\nu + \tilde{\nu})\frac{\partial \tilde{\nu}}{\partial x_j}\right) + c_{b2}\frac{\partial \tilde{\nu}}{\partial x_i}\frac{\partial \tilde{\nu}}{\partial x_i} + c_{c1} f_c \frac{\tilde{\nu}^2}{a^2} P_f\right] \tag{2}$$

The Menter 1-equation transition model is a single-equation transition model which determines boundary-layer transition based on a transport equation of the turbulence intermittency variable, γ, along with the momentum thickness, Re_θ, of the boundary-layer. Additional information about the Menter transition model can be found in [34]. The SA turbulence model is a single-equation model which solves for the turbulent eddy-viscosity ratio, $\tilde{\nu}$. It is assumed that the flow at the farfield inflow is laminar with a turbulent eddy-viscosity ratio of 0.01 (a commonly recommended choice for quiet wind tunnel applications). As the flow moves through the boundary-layer region, the turbulent eddy-viscosity ratio will change, possibly reaching a threshold where the Menter transition and SA turbulence model begin turbulent modeling of the boundary-layer region. The spatial accuracy for both the turbulence and transition model is second-order.

E. Wind Tunnel Experimental Methods

Experiments were carried out in the BAM6QT hypersonic wind tunnel at Purdue University. The BAM6QT is a blowdown tunnel that relies on diaphragm burst downstream of a converging-diverging nozzle to produce high-velocity flow in the test section. A polished converging-diverging nozzle along with a boundary-layer bleed apparatus helps to produce a laminar boundary-layer region leading up to the test section portion of the tunnel. A quiet freestream flow is highly desirable for studying surface heating and boundary-layer transition. The reduced tunnel noise helps to improve the accuracy of laminar and transitional experiments performed in the wind tunnel. More discussion about the BAM6QT experiments on the Talon-P is presented in [22].

III. Results and Discussion

The hypersonic glide vehicle geometry is a complex geometry which combines many components used in canonical hypersonic flow studies, such as: compression ramps, expansion corners, flat plates, fins, wings, etc. The combination of these structures gives rise to complex flow features which impact important design considerations such as surface heating, surface pressure, flight stability, and flow unsteadiness. This section will provide a discussion of the resulting flow features observed in simulated and experimental results, with special emphasis on analyzing how the geometry of the nose impacts the downstream flow behavior.

The heat flux contours on the top and bottom of the vehicle for the Baseline and the Sample 13 geometry are shown in Figs. 4 and 5. In these results, we generally see the highest heating intensity on sharp windwards surfaces; specifically on the leading edges of the nose, wings, and vertical stabilizer. Aside from these regions of interest, fin-root vortices

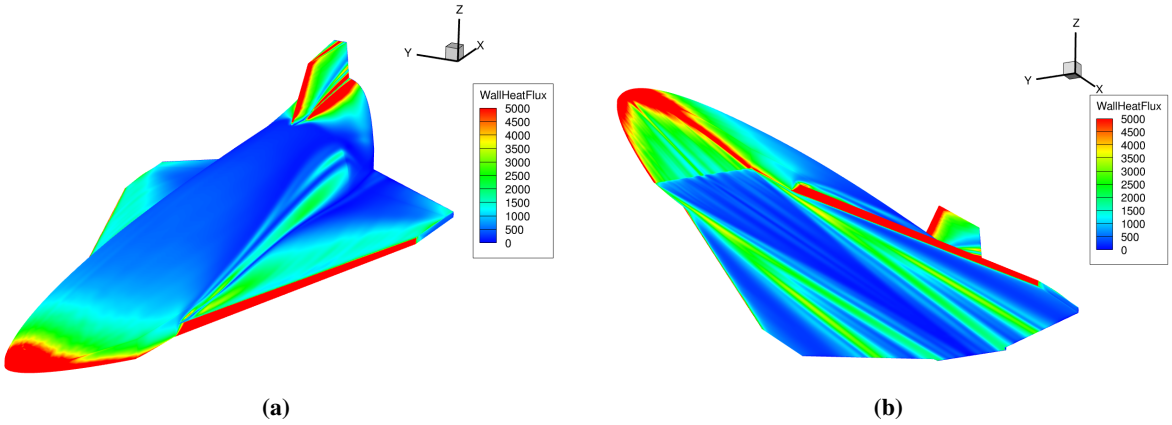

(a) **(b)**

Fig. 4 Baseline configuration. Contours of surface heating $[\mathrm{W/m^2}]$. (a) Top view. (b) Bottom view.

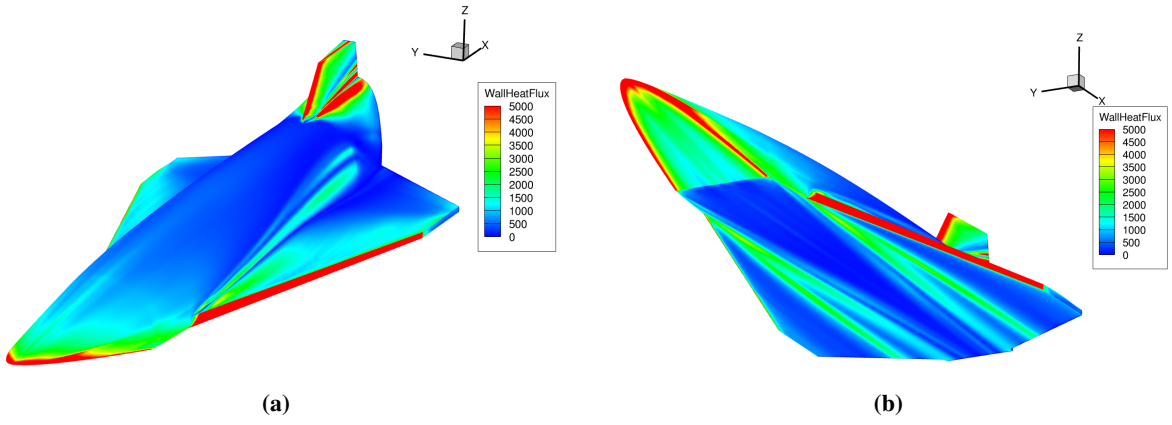

(a) **(b)**

Fig. 5 Sample 13 configuration. Contours of surface heating $[\mathrm{W/m^2}]$. (a) Top view. (b) Bottom view.

near the base of the vertical stabilizer give rise to intense surface heating streaks. The results displayed in Figures 4 and 5 demonstrate how changing the nose geometry has an impact on downstream flow properties. On the bottom surface of the baseline and Sample 13 vehicles, clear differences are visible in the surface heating contours, indicating a change in flow behavior near the body. To better understand these differences in steady-state flow behavior, Section III.A draw comparisons between simulated results obtained using KCFD and experimental results obtained in the BAM6QT. Section III.B will analyze limiting streamlines, vortical strucutres, and transitional flow behavior observed in the simulated results.

A. Comparison to Experimental Results

Figure 6 displays the three slice extraction locations on the bottom of the Baseline Talon-P geometry. The slices are extracted at $X = 161$ mm, $X = 199$ mm, and $X = 263$ mm. The nose-body juncture is the $X = 0.0$ mm location for all Talon-P configurations. These slice extraction locations were chosen to avoid artifacts seen in the experimental heat flux data due to PCB sensors placed at the surface.

Figures 7 to 12 display comparisons between the BAM6QT experimental results and the KCFD results. The extraction location is included in the title of each plot. The x-axis in each plot is Stanton number multiplied by the square root of the unit Reynolds number, and the y-axis is the spanwise distance from the centerline.

Figure 7 compares CFD predictions with wind tunnel measurements for the baseline nose geometry. For all three extraction locations, there is a reasonable agreement of peak locations in the spanwise direction. At the $X = 161.0$ mm and $X = 199.0$ mm extraction locations, the peaks located near $Y = \pm 30$ mm show excellent agreement. The peak magnitudes located at $Y = \pm 40$ mm disagree by roughly 20%. The uncertainty associated with the IR camera is approximately 20%, so this disagreement is still within expected uncertainties. A discrepancy is observed near the

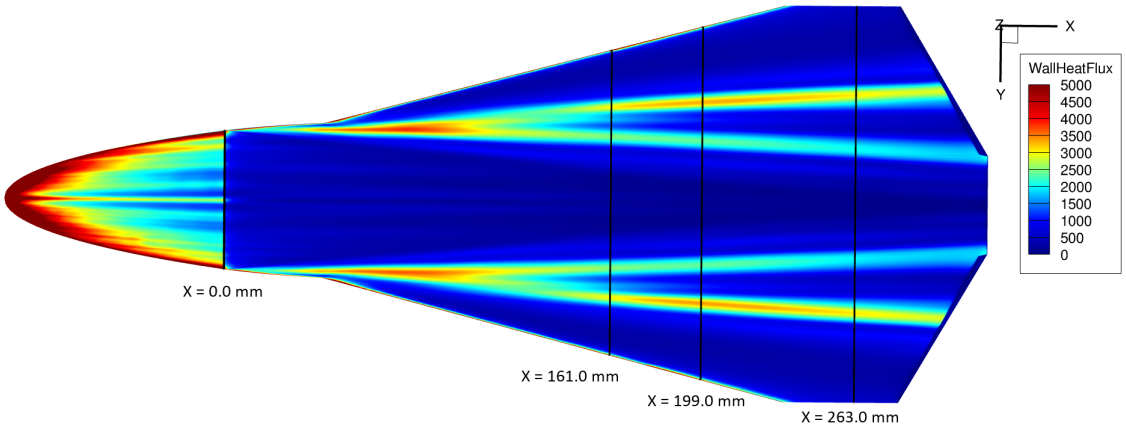

Fig. 6 Surface extraction locations and heat flux contours $[\mathrm{W/m^2}]$**.**

centerline ($Y = 0.0$ mm) for all three extraction locations. Centerline Stanton number discrepancies are observed in almost all of the plots displayed in Figures 7 to 12.

Figures 8 and 9 display the surface heating comparisons for the Sample 2 and 3 nose geometries. The peak locations in the spanwise direction match closely; however, the CFD results under-predict the peak Stanton number magnitude by more than 30% at some locations. The IR camera uncertainty is roughly 20%, which is insufficient to explain this discrepancy. It seems more likely that angle-of-attack uncertainty in the experiments, or computational issues are responsible for this discrepancy. The wind tunnel data also appear to be asymmetric near the centerline ($Y = 0.0$ mm) at the $X = 161.0$ mm extraction location for both the Sample 2 and 3 nose geometries. The exact reason for this asymmetry is unkown.

The extractions for Samples 9, 12, and 13 are shown in Figures 10 to 12. These three cases show overall good comparisons between the spanwise peak locations and peak Stanton number values. The experimental data at the $X = 161.0$ mm extraction location in Fig. 12 display a peak near the centerline. It is likely that this peak is due to the sharpness of the nose on the Sample 13 geometry (see Fig. 2).

Generally, the cases where two distinct heating streaks are observed (Samples 2 and 3) experience substantial disagreements between peak heating magnitudes, whereas cases with multiple distinct surface heating streaks (Baseline, Sample 9, Sample 12, and Sample 13) display better agreement between CFD and experimental results. From a validation standpoint, it is promising that the CFD predictions for the Baseline and Samples 9, 12, and 13 are generally within 20% of the experimental surface heating values. The difference in number of observed heating streaks is discussed further in subsection III.B.

It is difficult to pinpoint a single reason for the discrepancies observed in the Sample 2 and 3 cases (Figures 8 and 9); it is possible that the observed discrepancy is a combination of multiple factors. Seeing overall good agreement for the Baseline, Sample 9, Sample 12, and Sample 13 cases is promising; however, the substantial disagreement observed in the Sample 2 and 3 cases warrants investigation.

Previous studies have found that small changes in angle-of-attack can yield substantial changes in vortex-induced surface heating [35]. There is some uncertainty in the experimental angle-of-attack, and it seems plausible that a small positive angle-of-attack in the wind tunnel tests could lead to substantially higher surface heating when compared with CFD predictions. If the angle-of-attack was corrected, it is possible that the CFD would fall within the 20% uncertainty of the IR camera measurements. It has also been found in our own testing that the nose geometry and angle-of-attack have a substantial effect on whether the streamwise vortices on the bottom surface of the Talon-P originate from the nose, or from the root of the wing leading edge. These effects will be discussed further in subsection III.B.

Beyond angle-of-attack uncertainty, there are other factors which could lead to the observed discrepancies, such as: wind tunnel condition uncertainty, IR camera uncertainty, and computational imperfections. The meshes are unstructured and comprised of tetrahedral cells which are not flow-aligned; this will yield undesirable CFD performance regardless of mesh refinement. Given the small size of the model and relatively high cell count (for basic laminar/RANS calculations), it seems unlikely that further increasing the cell count would significantly improve the CFD predictions. Additionally, the calculated Δx^+, Δy^+, and Δz^+ values are well-within recommended values for laminar or RANS simulations, so it is unlikely that further refinement would yield better predictions.

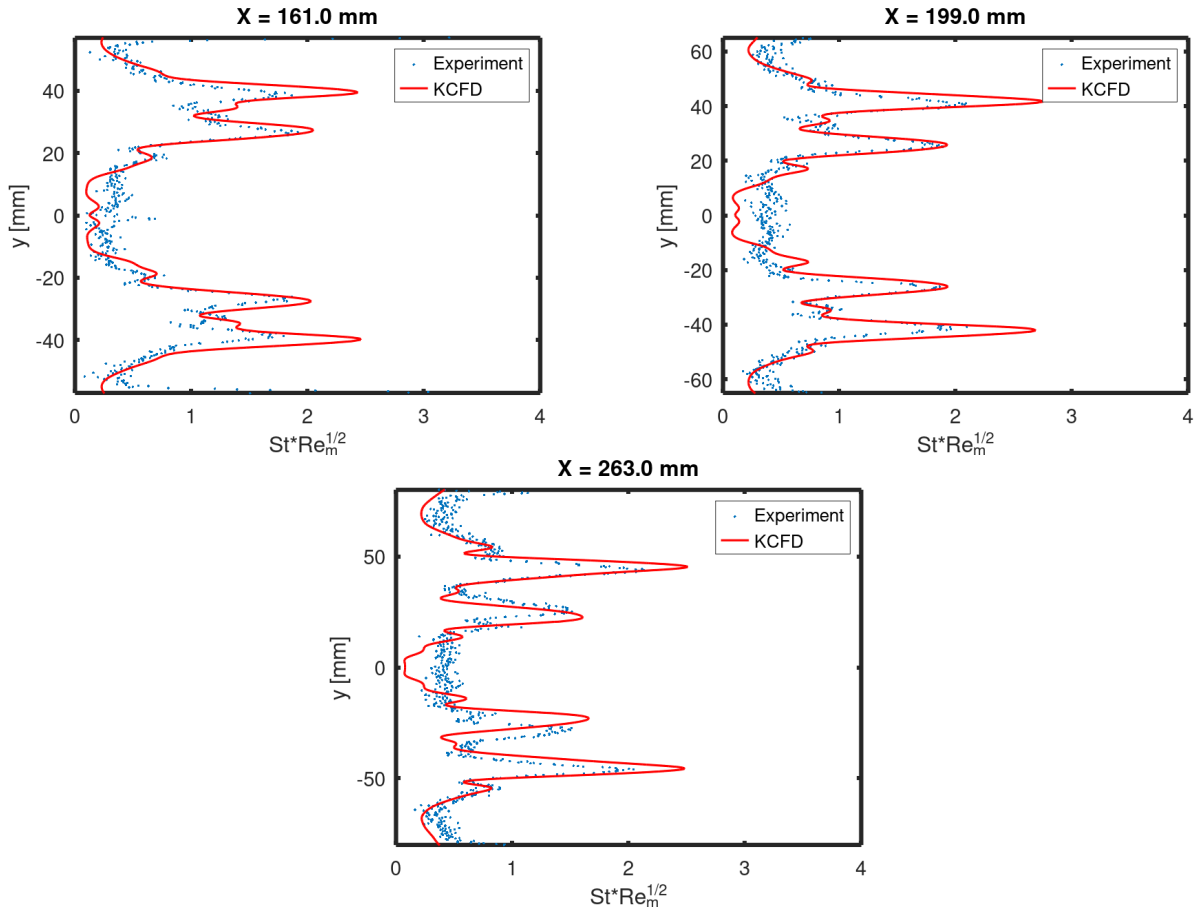

Fig. 7 Experimental and computational surface heating comparison. Baseline nose geometry.

The stagnation temperature of the BAM6QT is another source of experimental uncertainty. The sensor used to record the stagnation temperature of the tunnel is located at the furthest upstream end of the driver tube. While this provides a good approximation of the driver section temperature, it is not a perfect measurement given the extensive length of the driver section tube. While this adds to the uncertainty of the experimental results, it is also unlikely to fully explain the observed discrepancy between predictions and experiments.

The heating streak patterns seen in the CFD results are observed in wind tunnel and high-fidelity CFD results. Additionally, small changes made to the nose design produced substantial changes to the downstream vortex-surface heating on the bottom surface of the vehicle. Low-fidelity panel methods, such as CBAero or FOSTRAD, will not resolve these features; both CBAero and FOSTRAD predict a nearly constant heat flux across the entire bottom surface of the Talon-P. The inability to model vortical structures and shock-wave/boundary-layer interaction are two major drawbacks of panel methods. The surface heating in regions where vortices or shocks interact closely with the surface will observe a substantial rise in surface heating and skin friction, which may be several times higher than the surrounding surface. If the thermal protection system of the vehicle is designed to accommodate heating based only on panel method results, regions of vortex-surface and shock-surface interactions will likely overheat. For this reason, it is necessary to run a handful of high-fidelity CFD runs throughout the DTBF cycle to gather information about surface heating and identify problematic regions.

B. Laminar Simulation Results

This section analyzes laminar CFD simulation results to provide a better understanding of how the flow structure around the body influences the surface properties observed in experiments. Detachment, reattachment, and vortical structures are prominent flow features in many of hypersonic flow fields [36–42]. For all six nose geometries tested, prominent streamwise vortices are visible in both simulations and wind tunnel results. Two distinct surface heating patterns were

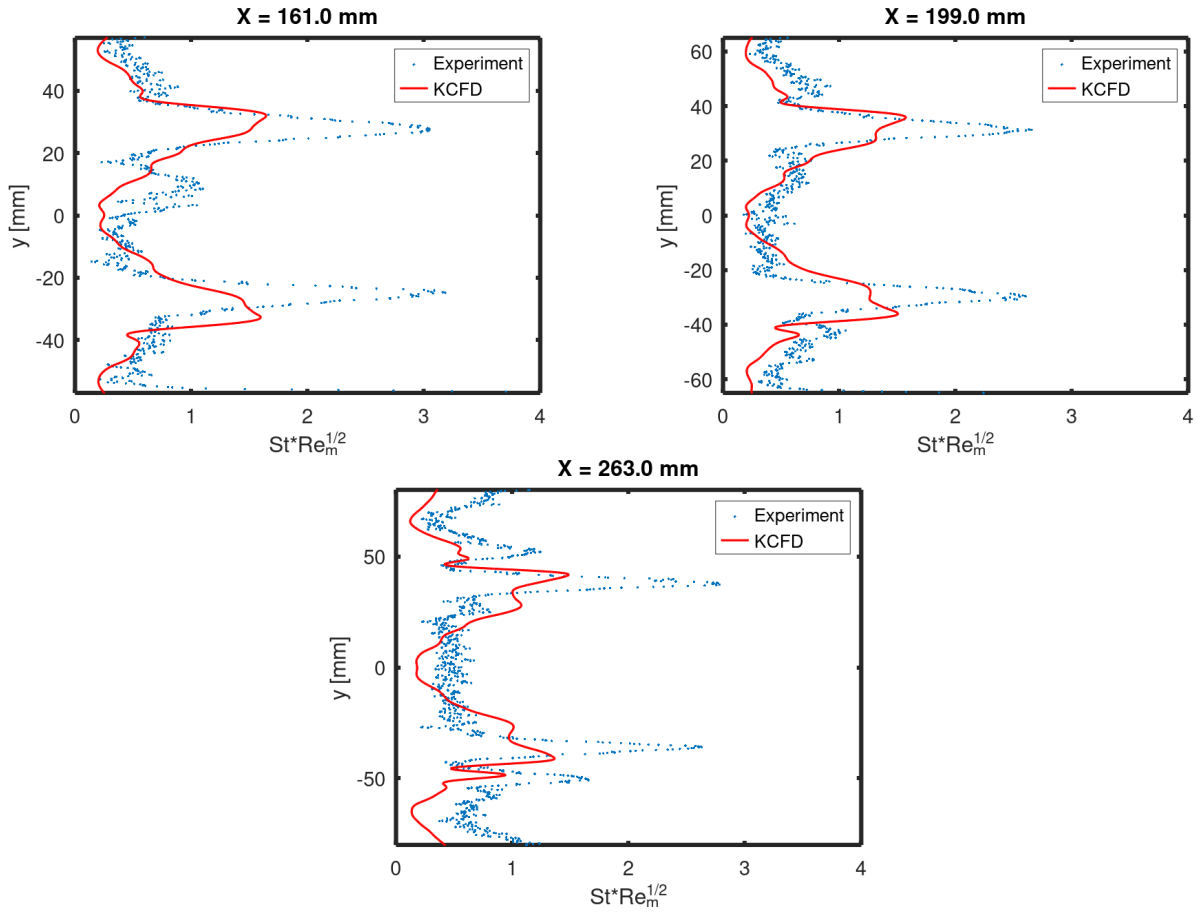

Fig. 8 Experimental and computational surface heating comparison. Sample 2 nose geometry.

noted: one with two distinct heating streaks originating at the nose (Sample 2 and 3), and another with multiple streaks originating from near the wing leading edge root (Baseline and Sample 9, 12, 13). The streamribbon plots presented in Fig. 13 and Fig. 14 demonstrate the difference in flow behavior which causes this phenomenon. Figure 13 displays streamribbons and surface heating on the baseline geometry and Fig. 14 displays streamribbons and surface heating on the Sample 2 geometry. In Fig. 13, the ribbons appear to begin near the nose tip on the upper surface, and eventually curl to the bottom surface near the nose/body junction. This is consistent with the heating patterns observed on the bottom of the Baseline geometry in Fig. 6. In Fig. 14, the ribbons curl from the top to bottom surface close to the nose tip, producing two heating streaks which begin at the nose and travel along the entire bottom surface. These two distinct flow behaviors appear to be caused by the compression ramp angle on the bottom surface of the nose (refer to Fig. 2). The small compression angle of the Sample 2 geometry results in a lower pressure on the bottom surface of the nose, which allows the high pressure air near the stagnation location to curl to the bottom surface almost immediately. The larger compression angle of the Baseline nose results in a higher pressure on the compression surface, which forces the flow to continue traveling on the top surface until further downstream, closer to the wing leading edge root location. This explanation also seems consistent for the other geometries, with Sample 3 (which has a shallow compression angle) observing similar flow behavior to Sample 2, and Samples 9, 12, and 13 (which have steeper compression angles) observing flow behavior similar to the Baseline geometry case. More discussion about the experimental results and the effect of the nose compression angle can be found in [22].

Vortical features are also observed at a few locations on the top surface of the vehicle. Above each wing, there is a large vortex which begins near the leading edge root and continues downstream along the upper surface of the Talon-P body. These voritces resulting from the wings can be seen in Figures 13 and 14 and the surface heating resulting from these vortices can be seen on the top surface in Figures 4 and 5. Additionally, heating effects from the fin-root vortices are visible near the base of the vertical stabilizer on the top surface in Figures 4 and 5. Different nose geometries did not

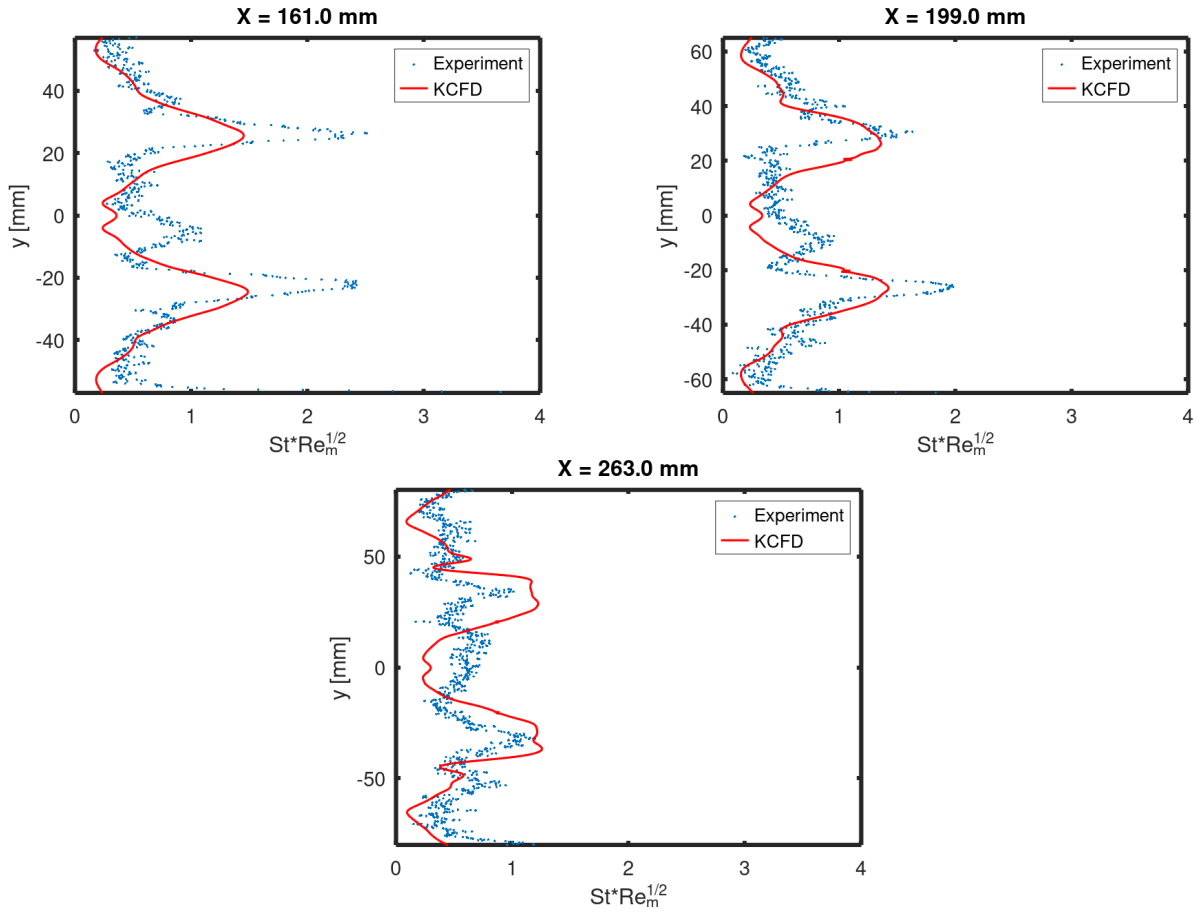

Fig. 9 Experimental and computational surface heating comparison. Sample 3 nose geometry.

appear to cause significant changes to heating patterns on the upper surface of the vehicle.

C. RANS Simulation Results

This section provides a brief discussion of issues encountered with transitional RANS CFD modeling on the Talon-P geometry. RANS simulations were performed in KCFD using the Menter 1-eqn transition model and the Spalart-Allmaras turbulence model. Transitional RANS models generally rely on one or more inflow turbulence parameters which are inferred based on previous experiments or wind tunnel noise time histories. The SA turbulence model relies on a single parameter, the freestream turbulent eddy-viscosity ratio, which was chosen to be 0.01 based on recommendations for quiet wind tunnel applications. Increasing this parameter forces earlier boundary-layer transition and decreasing this parameter delays transition.

Figure 15 displays the RANS surface heating results on the bottom of the Baseline Talon-P configuration. The laminar results appear to predict several well-defined heating streaks across the entirety of the bottom surface whereas the transitional RANS results appear to predict initial well-defined streaks which subsequently broaden into wider wedge-like shapes further downstream. Heat flux and skin friction measurements strongly indicate that the simulation predicts flow transition in the RANS simulations. Similar transition was observed for all nose geometries, with initially well-defined streaks in the laminar boundary-layer flow closer to the nose, and wide turbulent boundary-layer heating wedges forming further downstream. None of the experiments appeared to predict obvious transition on the bottom surface of the Talon-P for any of the nose geometries; thus, it seems reasonable to conclude that the Menter transition model is predicting boundary-layer transition much sooner than the experimental results. Based on these results, it seems likely that the freestream turbulent eddy-viscosity value of 0.01 is higher than the actual value in the BAM6QT. Additional experimental work and simulation work would be required to confirm this reasoning.

These results demonstrate a common issue encountered with RANS CFD modeling when making comparisons to

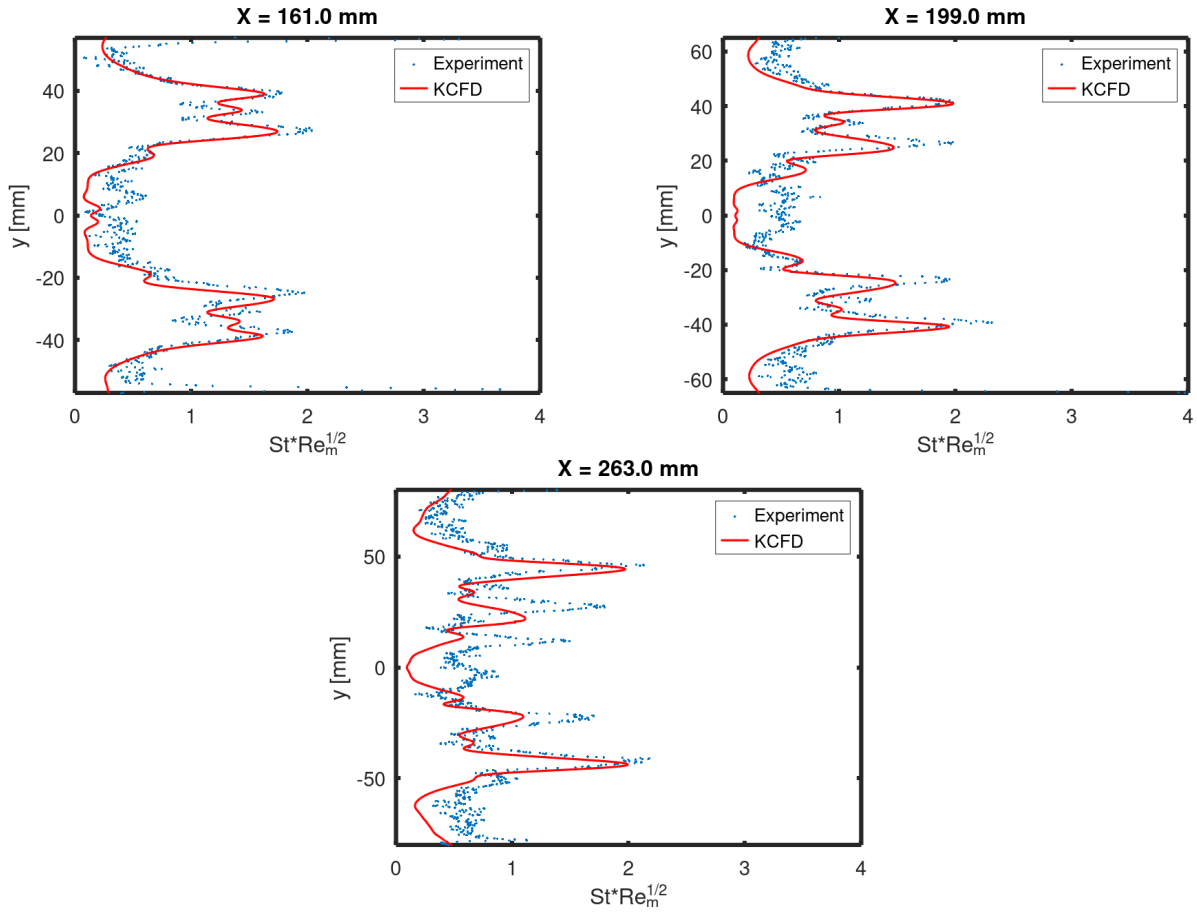

Fig. 10 Experimental and computational surface heating comparison. Sample 9 nose geometry.

ground-testing experimental work. Most existing turbulence and transition used in RANS modeling require knowledge of one or more freestream turbulence parameters in order to accurately model boundary layer transition. Generally, many RANS models require that some combination of freestream turbulent eddy-viscosity, turbulence intensity, turbulent kinetic energy, etc. be specified at the simulation inflow. Unlike LES and DNS, where boundary-layer transitional and turbulent structures are resolved to varying degrees, RANS modeling uses a combination of models in the near-wall region to model, rather than resolve, boundary-layer transition and turbulence. Depending on what values the user chooses for the aforementioned turbulence parameters, the transitional and turbulent boundary-layer behavior may change considerably. For turbulence models which rely on only one freestream turbulence parameter, such as the SA turbulence model, performing a sweep of possible turbulent eddy-viscosity values in the freestream to match experimental transition is feasible (but may be computationally expensive and time-intensive). For turbulence models which rely on two or more freestream turbulence parameters, the test matrix quickly becomes unreasonably large.

Even with considerable tuning of the simulations, there are no guarantees that the CFD results will match experimental results. In the authors' experience, geometric irregularities (such as gaps, fins, wings, sharp interfaces, etc.) can cause RANS transition and turbulence models to behave unpredictably. Matching experimental transition locations on the main vehicle body does not necessarily guarantee that transition will match experiments on the fins or wings of the vehicle. Increasing the geometric complexity of a flight vehicle generally causes greater misalignment between simulations and experiments.

Transition in hypersonic boundary-layers is a subject of ongoing research [35, 43–55]. It is generally understood that small perturbations in a laminar boundary-layer flow can lead to instability waves, and ultimately to turbulent breakdown; however, the exact transition process and flow behavior for complex, three-dimensional configurations like the Talon-P is an ongoing subject of investigation. The process of boundary-layer transition is sensitive to flow conditions, freestream noise, surface roughness, etc. and any changes in these conditions can significantly impact boundary-layer

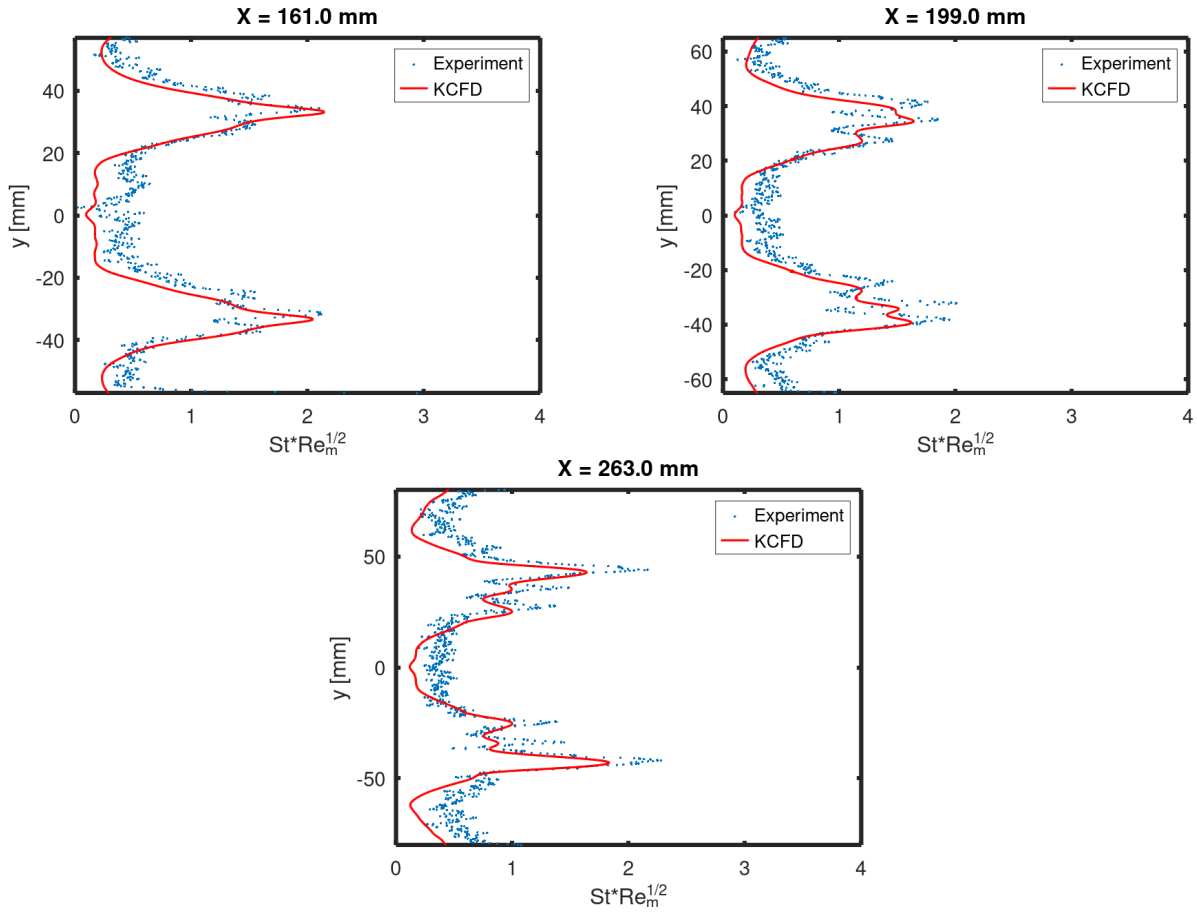

Fig. 11 Experimental and computational surface heating comparison. Sample 12 nose geometry.

transition behavior. For this reason, it is a challenge for both CFD and experiments to obtain perfect matches for transitional boundary-layer flow results. Future improvements in CFD RANS models, along with more precise methods of experimental measurements (i.e. surface roughness, wind tunnel noise), may yield better comparisons.

IV. Conclusion

In this project we analyzed flow over a generic HGV configuration, the Talon-P, using laminar CFD simulation methods. Simulated and experimental results were compared, demonstrating a reasonably close match between the results for most cases. For Sample 2 and Sample 3, substantial discrepancies were observed in the peak surface heating magnitudes. Some possible reasons for the discrepancies are suggested, with angle-of-attack uncertainty in the wind tunnel results and the tetrahedral mesh design highlighted as likely candidates. Future work may involve running the Sample 2 and Sample 3 nose geometries at small positive and negative angles-of-attack in CFD simulations to determine whether the experimental results fall within these bounding cases.

Future studies may run the BAM6QT in its ‘‘noisy’’ mode (as opposed to the ‘‘quiet’’ mode used for the wind tunnel results shown in this paper) to analyze boundary-layer transition and benchmark the capabilities of KCFD’s implementation of the Menter transition model. Obtaining accurate transition results is important for predicting drag and surface heating on hypersonic flight vehicles. Although boundary-layer transition was not observed in the experimental measurements discussed in this paper, a full-scale flight version of the Talon-P would likely observe transition at atmospheric flight conditions; it is also expected that noisy runs of the BAM6QT may produce boundary-layer transition on the Talon-P. Running time-accurate LES or DES simulations of the Talon-P may also be beneficial to capture unsteady flow behavior on the Talon-P.

Cross-validations between experiments and simulations also significantly improves confidence in results during the

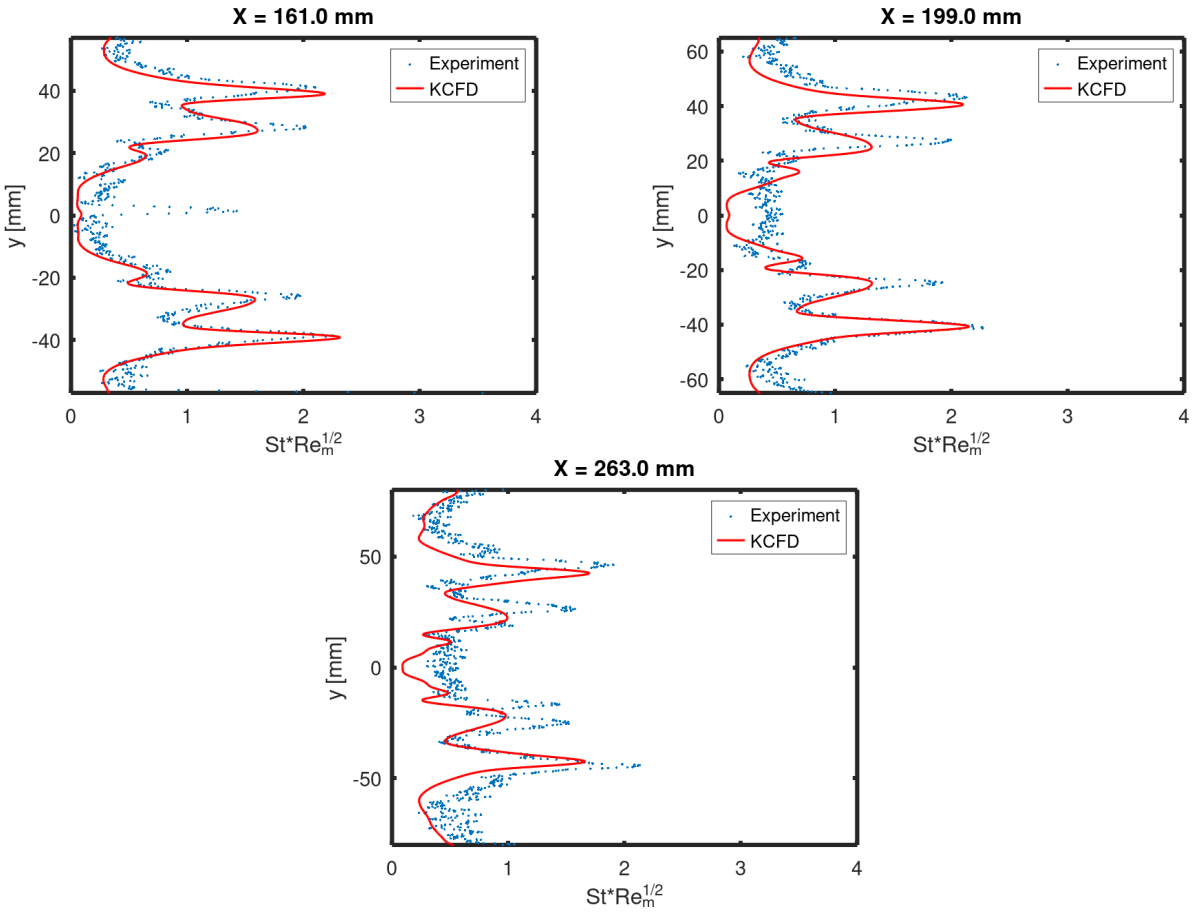

Fig. 12 Experimental and computational surface heating comparison. Sample 13 nose geometry.

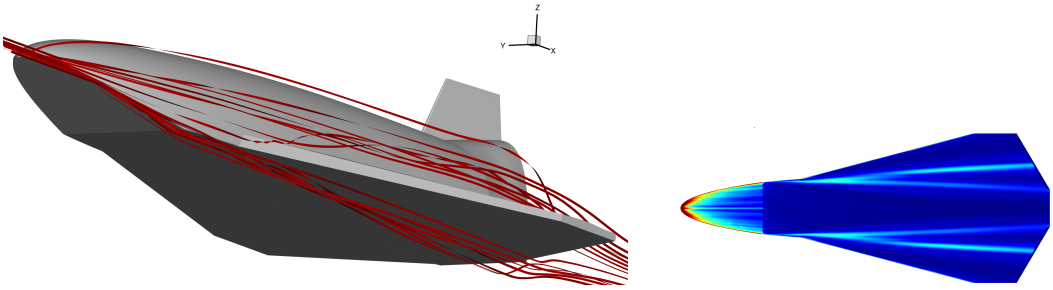

Fig. 13 Streamribbons (left) and bottom surface heating (right). Baseline nose geometry.

design process. Faulty results in experiments or simulations can happen for numerous reasons, several of which have been discussed in this paper. Showing a close comparisons between experiments and CFD simulations can help identify inaccurate results.

In the DTBF cycle, CFD can be used to predict flow behavior and drive design choices for the thermal protection system, control systems, propulsion systems, etc. High-fidelity CFD results provide detailed insight into the aerodynamic behavior of a given design without conducting expensive flight tests. While flight testing and ground testing primarily provide vehicle surface data, CFD can offer additional information on three-dimensional flow features to help explain steady and unsteady flow features observed in the flight/ground testing. In this paper, streamribbon plots helped to provide a reasonable justification for vortical structures seen in both the CFD simulations and experimental tests. Understanding why certain flow structures form can help designers to make better-informed decisions in future design

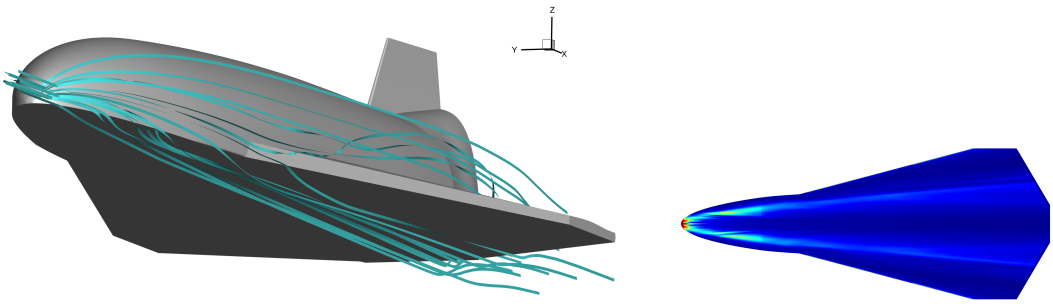

Fig. 14 Streamribbons (left) and bottom surface heating (right). Sample 2 nose geometry.

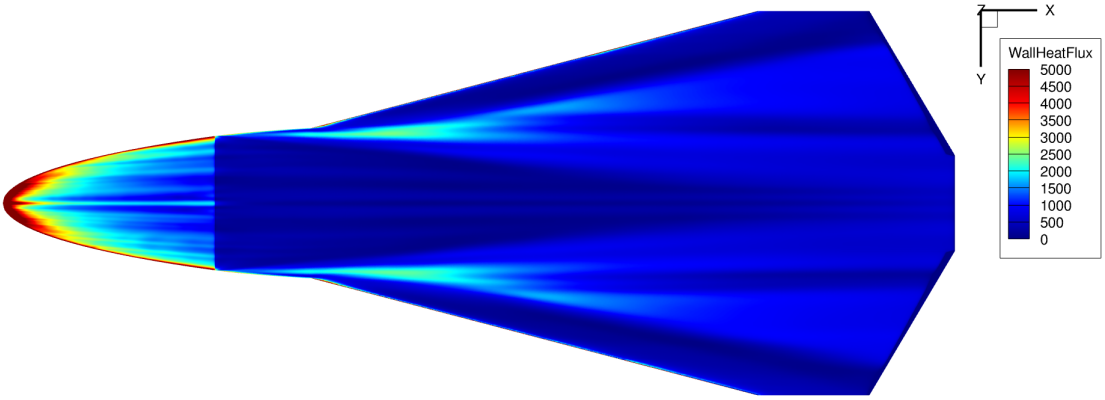

Fig. 15 RANS heat flux contours $[\mathrm{W/m^2}]$**.**

iterations. Rather than running a test matrix of every possible geometry, insights from CFD results can narrow the scope of adjustments that need to be made to the design. For example, if it is desirable to minimize interaction of vortices with the bottom surface of the Talon-P vehicle, the CFD results would guide us to choose a larger compression angle on the bottom surface of the nose (based on the results discussed in Section III.B). Further geometric adjustments could also be made to deflect the large vortical structures away from the bottom surface of the vehicle.

Acknowledgments

Funding for this project was provided by Stratolaunch LLC (J. Stults, technical monitor). The work was also supported by grants of high-performance computing time from the U.S. Department of Defense (DOD) High Performance Computing Modernization program at the DEVCOM-ARL DOD Supercomputing Resource Center (DSRC), Aberdeen Proving Ground, MD and the U.S. Army Engineer Research and Development Center DSRC, Vicksburg, MS. The authors are also indebted to Joseph Jewell, Brandon Chynoweth, and Samantha Miller for providing experimental data for comparison with the computational results.

References

[1] Gaitonde, D., ‘‘Progress in shock wave / boundary layer interactions,’’ AIAA 2013-2607. *43^{rd} Fluid Dynamics Conference.* June 2013. `https://doi.org/10.2514/6.2013-2607`.

[2] Dolling, D., ‘‘Fifty Years of Shock-Wave/Boundary-Layer Interaction Research: What Next?’’ *AIAA Journal*, Vol. 39, No. 8, 2001, pp. 1517,1531. https://doi.org/10.2514/2.1476.

[3] Babinsky, H., and Harvey, J., ‘‘Shock Wave-Boundary-Layer Interactions,’’ *Cambridge Aerospace Series*, 2011, pp. 5,373. https://doi.org/10.1017/CBO9780511842757.

[4] Bernardini, M., Asproulias, I., Larsson, J., Pirozzoli, S., and Grasso, F., ‘‘Heat transfer and wall temperature effects in shock

wave turbulent boundary layer interactions,'' *Physical Review Fluids*, Vol. 1, No. 8, 2016. https://doi.org/10.1103/PhysRevFluids.1.084403.

[5] Alviani, R., Poggie, J., and Blaisdell, G., ''Unsteady Aspects of Shock-Wave/Boundary-Layer Interaction Resulting from Control Surface Deflection,'' *AIAA Journal*, Vol. 60, No. 8, 2022, pp. 4649–4659. https://doi.org/10.2514/1.J061337.

[6] Clemens, N. T., and Narayanaswamy, V., ''Low-Frequency Unsteadiness of Shock Wave/Turbulent Boundary Layer Interactions,'' *Annual Review of Fluid Mechanics*, Vol. 46, No. 1, 2014, pp. 469–492. https://doi.org/10.1146/annurev-fluid-010313-141346.

[7] Leidy, A. N., Neel, I. T., Tichenor, N. R., and Bowersox, R. D. W., ''High-Speed Schlieren Imaging of Cylinder-Induced Hypersonic-Shock-Wave–Boundary-Layer Interactions,'' *AIAA Journal*, Vol. 58, No. 7, 2020, pp. 3090–3099. https://doi.org/10.2514/1.J059193.

[8] Holden, M., ''A review of aerothermal problems associated with hypersonic flight,'' AIAA 1986-267. 24^{th} *Aerospace Sciences Meeting*. January 1986. https://doi.org/10.2514/6.1986-267.

[9] Brusniak, L., and Dolling, D. S., ''Engineering estimation of fluctuating loads in shock wave/turbulent boundary-layer interactions,'' *AIAA Journal*, Vol. 34, No. 12, 1996, pp. 2554–2561. https://doi.org/10.2514/3.13438.

[10] Sandham, N., Schülein, E., Wagner, A., Willems, S., and Steelant, J., ''Transitional shock-wave/boundary-layer interactions in hypersonic flow,'' *Journal of Fluid Mechanics*, Vol. 752, 2014, pp. 349–382. https://doi.org/10.1017/jfm.2014.333.

[11] Alviani, R., Fano, D., Poggie, J., and Blaisdell, G., ''Aerodynamic Heating in the Gap Between a Missile Body and a Control Fin,'' *Journal of Spacecraft and Rockets*, Vol. 59, No. 4, 2022, pp. 1111–1124. https://doi.org/10.2514/1.A35183.

[12] Gaitonde, D. V., and Adler, M. C., ''Dynamics of Three-Dimensional Shock-Wave/Boundary-Layer Interactions,'' *Annual Review of Fluid Mechanics*, Vol. 55, No. 1, 2023, pp. 291–321. https://doi.org/10.1146/annurev-fluid-120720-022542.

[13] Adler, M. C., and Gaitonde, D. V., ''Flow Similarity in Strong Swept-Shock/Turbulent-Boundary-Layer Interactions,'' *AIAA Journal*, Vol. 57, No. 4, 2019, pp. 1579–1593. https://doi.org/10.2514/1.J057534.

[14] Adler, M. C., and Gaitonde, D. V., ''Dynamics of strong swept-shock/turbulent-boundary-layer interactions,'' *Journal of Fluid Mechanics*, Vol. 896, 2020, p. A29. https://doi.org/10.1017/jfm.2020.334.

[15] Stetson, K., Thompson, E., Donaldson, J., and Siler, L., ''Laminar boundary layer stability experiments on a cone at Mach 8. III - Sharp cone at angle of attack,'' AIAA 1985-492. 23^{rd} *Aerospace Sciences Meeting*. January 1985. https://doi.org/10.2514/6.1985-492.

[16] McCabe, A., ''The Three-Dimensional Interaction of a Shock Wave with a Turbulent Boundary Layer,'' *Aeronautical Quarterly*, Vol. 17, No. 3, 1966, p. 231–252. https://doi.org/10.1017/S0001925900003851.

[17] Schmisseur, J. D., and Gaitonde, D. V., ''Numerical Investigation of Strong Crossing Shock-Wave/Turbulent Boundary-Layer Interactions,'' *AIAA Journal*, Vol. 39, No. 9, 2001, pp. 1742–1749. https://doi.org/10.2514/2.1504.

[18] Gaitonde, D., Shang, J. S., and Visbal, M., ''Structure of a double-fin turbulent interaction at high speed,'' *AIAA Journal*, Vol. 33, No. 2, 1995, pp. 193–200. https://doi.org/10.2514/3.12449.

[19] Prasad, C., and Gaitonde, D., ''Turbulence Modeling of High-speed Flows with Upstream-Informed Corrections,'' , 05 2022. https://doi.org/10.48550/arXiv.2205.15377.

[20] Ma, J., Liu, Y., Liu, Y., and Shi, J., ''Heat flux measurement at hypersonic turbulent separated flow field induced by the blunt fins,'' *Journal of Physics: Conference Series*, Vol. 2882, No. 1, 2024, p. 012099. https://doi.org/10.1088/1742-6596/2882/1/012099.

[21] Mortazavi, M., and Knight, D., ''Simulation of Hypersonic-Shock-Wave–Laminar-Boundary-Layer Interaction over Blunt Fin,'' *AIAA Journal*, Vol. 57, No. 8, 2019, pp. 3506–3523. https://doi.org/10.2514/1.J057940.

[22] Miller, S., Dean, M., Carpenter, D., Chynoweth, B., and Jewell, J., ''Talon-P: Experimental Investigation of the Talon-P Geometry in Mach 6 Quiet Flow,'' *AIAA Aviation Forum*, 2025.

[23] Zhao, Z.-T., Huang, W., Yan, L., and guang Yang, Y., ''An overview of research on wide-speed range waverider configuration,'' *Progress in Aerospace Sciences*, Vol. 113, 2020, p. 100606. https://doi.org/https://doi.org/10.1016/j.paerosci.2020.100606.

[24] Townend, L., ''Research and design for lifting reentry,'' *Progress in Aerospace Sciences*, Vol. 19, 1979, pp. 1–80. https://doi.org/https://doi.org/10.1016/0376-0421(79)90001-0.

[25] Huang, W., Ma, L., guo Wang, Z., Pourkashanian, M., Ingham, D. B., bin Luo, S., and Lei, J., ''A parametric study on the aerodynamic characteristics of a hypersonic waverider vehicle,'' *Acta Astronautica*, Vol. 69, No. 3, 2011, pp. 135–140. https://doi.org/https://doi.org/10.1016/j.actaastro.2011.02.016.

[26] Cadence Design Systems Inc., ''Pointwise Meshing,'' , 2023.

[27] Department of Defense High Performance Computing Modernization Project, *Kestrel User Manual version 12.6.1*, 2023.

[28] McDaniel, D. R., and Tuckey, T., ''HPCMP CREATE^{TM}-AV Kestrel New and Emerging Capabilities,'' AIAA 2020-1525. *AIAA Scitech 2020 Forum.* January 2020. https://doi.org/10.2514/6.2020-1525.

[29] Nishikawa, H., Nakashima, Y., and Watanabe, N., ''Effects of High-Frequency Damping on Iterative Convergence of Implicit Viscous Solver,'' *Journal of Computational Physics*, Vol. 348, 2017. https://doi.org/10.1016/j.jcp.2017.07.021.

[30] McDaniel, D. R., Nichols, R. H., Eymann, T. A., Starr, R. E., and Morton, S. A., ''Accuracy and Performance Improvements to Kestrel's Near-Body Flow Solver,'' AIAA 2016-1051. *54th AIAA Aerospace Sciences Meeting*. January 2016. https://doi.org/10.2514/6.2016-1051.

[31] Anderson, M., Cooley, K., DeSpirito, J., and Schnepf, C., ''The Influence of the Numerical Scheme in Predictions of Vortex Interaction about a Generic Missile Airframe,'' AIAA 2022-1178. *AIAA SCITECH 2022 Forum.* January 2022. https://doi.org/10.2514/6.2022-1178.

[32] Spalart, P., and Allmaras, S., ''A One-Equation Turbulence Model for Aerodynamic Flows,'' AIAA 1992-439. *30th Aerospace Sciences Meeting and Exhibit.* January 1992. https://doi.org/10.2514/6.1992-439.

[33] Nichols, R. H., *A Summary of the Turbulence Models in the CREATE-AV Kestrel Flow Solvers*, 2019. https://doi.org/10.2514/6.2019-1342.

[34] Menter, F., Smirnov, P., Liu, T., and Avancha, R., ''A One-Equation Local Correlation-Based Transition Model,'' *Flow, Turbulence and Combustion*, Vol. 95, 2015. https://doi.org/10.1007/s10494-015-9622-4.

[35] Wirth, J. M., ''Measurement of Surface Heat Flux Due to Fin-Induced Shock-Boundary Layer Interactions,'' 2021. https://doi.org/1969.1/196393.

[36] Zukoski, E. E., and Spaid, F. W., ''Secondary injection of gases into a supersonic flow,'' *AIAA Journal*, Vol. 2, No. 10, 1964, pp. 1689–1696. https://doi.org/10.2514/3.2653.

[37] Shang, J. S., McMaster, D. L., Scaggs, N., and Buck, M., ''Interaction of jet in hypersonic cross stream,'' *AIAA Journal*, Vol. 27, No. 3, 1989, pp. 323–329. https://doi.org/10.2514/3.10115.

[38] Fric, T. F., and Roshko, A., ''Structure in the Near Field of the Transverse Jet,'' *Turbulent Shear Flows 7*, Springer Berlin Heidelberg, Berlin, Heidelberg, 1991, pp. 225–237. https://doi.org/10.1007/978-3-642-76087-7_17.

[39] Kelso, R. M., and Smits, A. J., ''Horseshoe vortex systems resulting from the interaction between a laminar boundary layer and a transverse jet,'' *Physics of Fluids*, Vol. 7, No. 1, 1995, pp. 153–158. https://doi.org/10.1063/1.868736.

[40] Munuswamy, N., and Govardhan, R., ''Shock wave boundary layer interactions in sonic gas jet injection into supersonic crossflow,'' *Experiments in Fluids*, Vol. 63, 2022. https://doi.org/10.1007/s00348-022-03488-5.

[41] Adler, M. C., and Gaitonde, D. V., ''Influence of separation structure on the dynamics of shock/turbulent-boundary-layer interactions,'' *Theoretical and Computational Fluid Dynamics*, Vol. 36, No. 2, 2022, pp. 303–326. https://doi.org/10.1007/s00162-021-00590-y.

[42] Reshotko, E., and Tucker, M., *Effect of a discontinuity on turbulent boundary-layer-thickness parameters with application to shock-induced separation*, National Advisory Committee for Aeronautics technical note ; NACA TN 3454, National Advisory Committee for Aeronautics, Washington, D.C, 1955.

[43] Johnson, H., Alba, C., Candler, G., MacLean, M., Wadhams, T., and Holden, M., ''Boundary-Layer Stability Analysis of the Hypersonic International Flight Research Transition Experiments,'' *Journal of Spacecraft and Rockets*, Vol. 45, No. 2, 2008, pp. 228–236. https://doi.org/10.2514/1.31878.

[44] Wadhams, T. P., Mundy, E., MacLean, M. G., and Holden, M. S., ''Ground Test Studies of the HIFiRE-1 Transition Experiment Part 1: Experimental Results,'' *Journal of Spacecraft and Rockets*, Vol. 45, No. 6, 2008, pp. 1134–1148. https://doi.org/10.2514/1.38338.

[45] MacLean, M., Wadhams, T., Holden, M., and Johnson, H., ''Ground Test Studies of the HIFiRE-1 Transition Experiment Part 2: Computational Analysis,'' *Journal of Spacecraft and Rockets*, Vol. 45, No. 6, 2008, pp. 1149–1164. https://doi.org/10.2514/1.37693.

[46] Johnson, H., and Candler, G., ''Hypersonic Boundary Layer Stability Analysis Using PSE-Chem'', AIAA 2005-5023. *35th AIAA Fluid Dynamics Conference and Exhibit.* June 2005. https://doi.org/10.2514/6.2005-5023.

[47] Herbert, T., ''Boundary-layer Transition - Analysis and Prediction Revisited'', AIAA 1991-737. *29th Aerospace Sciences Meeting*. January 1991. https://doi.org/10.2514/6.1991-737.

[48] Malik, M. R., ''Prediction and Control of Transition in Supersonic and Hypersonic Boundary Layers,'' *AIAA Journal*, Vol. 27, No. 11, 1989, pp. 1487–1493. https://doi.org/10.2514/3.10292.

[49] Malik, M. R., ''Hypersonic Flight Transition Data Analysis Using Parabolized Stability Equations with Chemistry Effects,'' *Journal of Spacecraft and Rockets*, Vol. 40, No. 3, 2003, pp. 332–344. https://doi.org/10.2514/2.3968.

[50] Stilla, J., ''Engineering transition prediction for a hypersonic axisymmetric boundary layer,'' *Journal of Aircraft*, Vol. 31, No. 6, 1994, pp. 1358–1364. https://doi.org/10.2514/3.46659.

[51] Di Renzo, M., and Urzay, J., ''Direct numerical simulation of a hypersonic transitional boundary layer at suborbital enthalpies,'' *Journal of Fluid Mechanics*, Vol. 912, 2021, p. A29. https://doi.org/10.1017/jfm.2020.1144.

[52] Fu, L., Karp, M., Bose, S. T., Moin, P., and Urzay, J., ''Shock-induced heating and transition to turbulence in a hypersonic boundary layer,'' *Journal of Fluid Mechanics*, Vol. 909, 2021, p. A8. https://doi.org/10.1017/jfm.2020.935.

[53] Holifield, L. H., ''Predicting Heating Rates in Hypersonic Gap Flows,'' 2022. https://doi.org/10.25394/PGS.20394504.v1.

[54] Currao, G. M. D., Choudhury, R., Gai, S. L., Neely, A. J., and Buttsworth, D. R., ''Hypersonic Transitional Shock-Wave–Boundary-Layer Interaction on a Flat Plate,'' *AIAA Journal*, Vol. 58, No. 2, 2020, pp. 814–829. https://doi.org/10.2514/1.J058718.

[55] Novikov, A. V., and Egorov, I., ''Direct Numerical Simulations of Transitional Boundary Layer over a Flat Plate in Hypersonic Free-Stream'', AIAA 2016-3952. *46th AIAA Fluid Dynamics Conferenc.* June 2016. https://doi.org/10.2514/6.2016-3952.